Touchless Electrostatic Detumbling of Differentially Charged Spacecraft in Geosynchronous Earth Orbit

Ethan M. Weber* and Hanspeter Schaub†
University of Colorado Boulder, Boulder, Colorado 80303

Electrostatic detumbling is a promising method for touchlessly detumbling large, uncooperative spacecraft in geosynchronous Earth orbit (GEO). Prior work has primarily considered fully conducting targets where the outer surface has a uniform electric potential. However, many legacy spacecraft have electrically isolated conducting components that can charge to largely different electric potentials from the rest of the spacecraft. Such differential potentials can significantly alter the electrostatic interactions between a tumbling target and servicer during proximity operations, potentially yielding more favorable torques during electrostatic detumbling. This paper develops and evaluates an active differential-charge control strategy that uses an electron-beam and targeted UV light source onboard a box-wing servicer spacecraft to produce controllable voltage differentials a target modeled after the GOES-R spacecraft. A Surface Multi-Sphere Model (SMSM) is used with an analytic charging model to calculate the coupled, steady-state voltages for various charge control modes. These voltages are then used with an SMSM electrostatic torque model and a Lyapunov-optimal control law to simulate electrostatic detumbling. Detumbling simulations are performed for both uniform and differential voltage cases under typical GEO space-weather conditions, and results show that differential voltage control reduces detumbling time from approximately 450 hours for the uniform case to about 300 hours for the studied geometry and an initial spin of 2 deg/s. These findings demonstrate that active differential charging can enhance electrostatic torques during detumbling and substantially shorten detumble times.

I. Nomenclature

I = Current on a conducting element (A).
Φ = Electric potential / Voltage (V).
$[S]$ = Elastance matrix (V/C).
Q = Charge (C).
ϵ_0 = Permittivity of free space ($\mathrm{F\,m^{-1}}$).
R_i = Radius of the ith SMSM sphere (m).
r_{ij} = Distance between SMSM spheres i and j (m).
$\mathbf{F}_i$ = Coulomb force on sphere i (N).
$\mathbf{r}_{c,i}$ = Vector from spacecraft center of mass to sphere i (m).
$\mathbf{L}_c$ = Electrostatic torque about center of mass (N m);
$\boldsymbol{\omega}$ = Angular rate (rad/s).
$[\tilde{\omega}]$ = Skew-symmetric matrix of $\boldsymbol{\omega}$.
$\boldsymbol{\beta}$ = Scalar-first quaternion.
$[I]$ = Moment of inertia matrix (kg$\cdot m^2$).
$V(\boldsymbol{\omega})$ = Lyapunov function.

---

*Graduate Research Assistant, Ann and H. J. Smead Department of Aerospace Engineering Sciences, 431 UCB, Colorado Center for Astrodynamics Research, Boulder, CO 80303; Student Member AIAA.

†Distinguished Professor and Department Chair, Ann and H. J. Smead Department of Aerospace Engineering Sciences, 431 UCB, Colorado Center for Astrodynamics Research, Boulder, CO 80303; Fellow AIAA

II. Introduction

The accumulation of non-compliant and derelict satellites in Geosynchronous Earth Orbit (GEO) presents a growing risk of collision events that could threaten critical space-based systems [1, 2]. To remedy this, numerous active debris removal (ADR) methods have been proposed in recent years to move debris objects from GEO to graveyard orbits. Most of these methods rely on physical contact between a servicer spacecraft and the target debris object through robotic arms, harpoons, nets, or mechanical grappling techniques to capture and relocate debris. While these methods are promising for capturing slowly rotating or controlled targets, they face significant momentum transfer and collision risks when attempting to capture objects in an uncontrolled tumble with high rotational kinetic energy [3–5]. This raises a considerable challenge for GEO debris removal where derelict spacecraft have been observed with spin rates ranging from 1-2deg/s to tens of degrees per second [6].

Electrostatic detumbling offers a touchless alternative to contact-based capture methods by using electrostatic torques between the tumbling target and a servicer spacecraft to achieve detumbling. In this technique, the servicer uses an electron-beam to control the electrostatic potential of itself and the target and produce Coulomb forces and torques that optimally reduce the rotational kinetic energy of the target [7–9]. Prior work exploring the electrostatic detumbling concept assumes the target spacecraft is fully conducting and all components therefore share a single electric potential. While modern guidelines for spacecraft design recommend that all surfaces of a spacecraft be fully conducting this guidance is not always followed. Many older spacecraft have electrically disconnected surfaces resulting in varying electric potentials across a spacecraft's components, a phenomenon known as differential charging [10, 11]. Depending on the magnitude of the differential potentials and the location of these electrically isolated surfaces, this differential charging can cause shifts in the center of charge (CoC) of the spacecraft relative to center of mass, potentially leading to larger electrostatic torques during proximity operations.

Recent advances in differential charge sensing [12] and targeted photoemission using UV lasers [13] motivate revisiting the electrostatic detumbling concept while considering spacecraft with differential voltage distributions. Focused UV illumination can drive an electrically isolated surface to a more positive potential by inducing photoelectron emissions, while an electron-beam can inject negative charge to other components, enabling control of the differential potential of the target spacecraft. An illustration of this concept is shown in Figure 1 where the right solar panel of the target is electrically insulated from the rest of the spacecraft. In this illustration, a focused UV lamp is used to produce photoelectron current in the isolated solar panel, charging it more positively than the rest of the spacecraft, while an electron-beam is used to provide a negative current to all target spacecraft components.

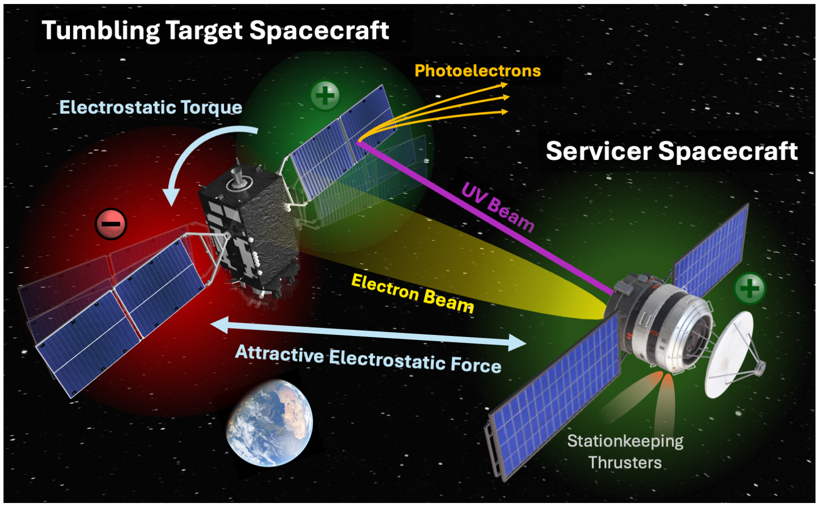

Fig. 1 Differential electrostatic detumbling concept using Electron Beam and UV Illumination.

This work develops and evaluates an active differential charge control strategy for electrostatic detumbling of a target spacecraft modeled after the GOES-R spacecraft in a GEO orbit. A Surface Multi-Sphere Model (SMSM) matched to a Method-of-Moments reference is used to compute elastances between electrically isolated components, and analytic current models are applied to determine steady-state potentials under various electron-beam and UV-light control modes. These voltages are then use with an SMSM-based electrostatic torque model and a Lyapunov-optimal voltage control law to simulate detumbling dynamics.

III. Problem Setup

This work considers the touchless, electrostatic detumbling of an uncontrolled target by a spacecraft equipped with an electron-beam and a targeted UV light source. The target spacecraft is modeled after the GOES-R spacecraft and consists of a bus, including an attached magnetometer boom, and a solar panel. The servicer is modeled as a box-wing spacecraft and is assumed to be a single conductive body. Using its electron-beam and UV light source, the servicer spacecraft can induce both positive and negative currents on the target spacecraft, controlling its electric potential distribution and varying the electrostatic torques between the target and servicer. The spacecraft are in a standard GEO orbit with a radius of 42,164 km with the servicer following the target at a constant 30 meter offset in the negative along-track direction.

To compare the performance of uniform and differential electrostatic detumbling, two charging scenarios are considered: (1) a *uniform target potential case*, where the target bus, and panel are electrically connected and therefore share a single potential, and (2) a *differential target potential case*, where the target panel is electrically isolated from the target bus, allowing it to acquire different electrical potentials. These two cases are shown in Fig. 2 where different colors represent electrically isolated bodies.

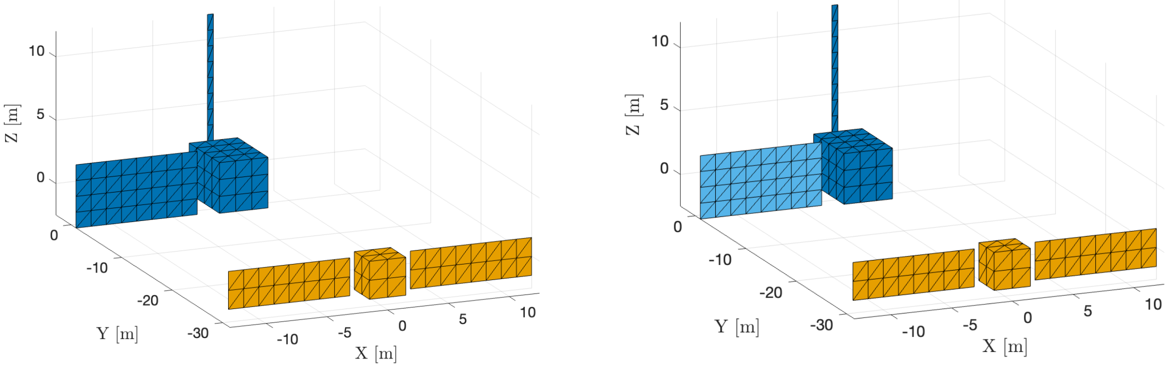

(a) Uniform Voltage Distribution Case

(b) Differential Voltage Distribution Case

Fig. 2 Electrostatic Detumbling Voltage Distribution Cases

IV. Methods

A. Differential Charging Model

Each electrically isolated component of the target-servicer system accumulates charge due to a combination of natural plasma currents, solar-UV-induced photoemission, electron-beam currents, and UV-beam induced photoelectron emission [14]. The evolution of the currents acting on each electrically isolated component is governed by the net current balance, given by

$$\frac{\mathrm{d}Q}{\mathrm{d}t} = I_e(\Phi) + I_i(\Phi) + I_{\mathrm{ph}}(\Phi) + I_{\mathrm{UV}}(\Phi) + I_{\mathrm{Beam}}(\Phi) + I_{\mathrm{SEE}}(\Phi) + I_{\mathrm{BSE}}(\Phi) \tag{1}$$

where the current terms correspond respectively to (in the order they appear in the equation) ambient electron collection, ambient ion collection, solar-UV-induced photoelectron emission, UV-beam–induced photoelectron emission, primary electron-beam current, and secondary and backscattered electron currents generated by electron-beam impact[14]. Excluding the UV-beam-induced current, all charging currents in Eq. (1) are based on analytic models implemented in Reference [15]. Because the spacecraft charging model is not the primary contribution of this work, the mathematical current formulation and models are not repeated here, and the reader is referred to [15] for the full set of current equations. In this study, the charging framework is extended by (1) applying it to a elastance model with multiple disconnected target components to capture differential charging across spacecraft surfaces, and (2) adding targeted UV-beam emission for differential potential control.

UV-Beam-Induced Photoelectron Current

The UV-beam produces photoelectrons by illuminating electrically isolated components of the target spacecraft. The number of emitted photoelectrons depends on both the incident photon flux and the material's photoelectric response, characterized by the quantum yield $Y(\hbar\omega)$, which represents the number of emitted electrons per incident photon with photon energy $\hbar\omega$ at normal incidence. The photon flux Φ_γ (photons per second) emitted by a UV source of optical power P_{UV} and photon energy $\hbar\omega$ (eV) is given by

$$\Phi_\gamma = \frac{P_{\text{UV}}}{\hbar\omega} \tag{2}$$

Using the quantum yield and photon flux, the total photoelectron current induced by a UV light source with energy $\hbar\omega$ impacting a spacecraft with a zero potential is given by

$$I_{\text{UV},0} = q_e\,\Phi_\gamma\,Y(\hbar\omega) \tag{3}$$

where q_e is the elementary charge [14]. For simplicity, this model does not consider surface reflectance or incidence angle, but future work plans to include these based on the formulation in Chapter 7 of [14]. The actual photoelectric current leaving the surface depends on the local electric potential Φ of the target component. For a positively charged surface, photoelectrons must overcome an electrostatic potential barrier to escape, resulting in an exponential suppression of the emitted current:

$$I_{\text{UV}}(\Phi) = I_{\text{UV},0}\exp\left(-\frac{\Phi}{T_{\text{UV}}}\right), \tag{4}$$

where T_{UV} is the mean kinetic energy of the emitted photoelectrons, assumed to be 2 eV in this work.

Differential Voltage Calculation

The electric potential of each electrically isolated component is related to the charge on the component through

$$\boldsymbol{\Phi} = [S]\boldsymbol{Q} \tag{5}$$

where $\boldsymbol{\Phi}$ is the vector of the electric potentials of each isolated conducting body (target bus, target panel, and servicer in the differential case), $\boldsymbol{Q}$ contains the corresponding total charge on each conducting body, and $[S]$ is the elastance matrix between these bodies. In the uniform-potential case, the target bus and panel are treated as a single conductor, and therefore share one electric potential in $\boldsymbol{\Phi}$. In the differential-potential case, they are treated as electrically isolated, giving each its own distinct voltage. This structural change in $[S]$ enables differential charging analysis.

Taking the derivative of both sides with respect to time yields relationship between current and the rate of change of each spacecraft potential, shown in

$$\frac{\mathrm{d}\boldsymbol{\Phi}}{\mathrm{d}t} = [S]\frac{\mathrm{d}\boldsymbol{Q}}{\mathrm{d}t} + \frac{\mathrm{d}[S]}{\mathrm{d}t}\boldsymbol{Q} \tag{6}$$

In this work, the differential charging analysis is performed assuming a quasi-static relative orientation between the target and servicer such that $\mathrm{d}[S]/\mathrm{d}t = 0$. Although the attitude motion during detumbling does induce variations in the elastance matrix, these changes occur on a slower timescale than it takes for charging to reach equilibrium. Thus the steady-state voltages are computed for representative static orientations to provide a reasonable approximation of the achievable potential differences during detumbling. Incorporating fully orientation-dependent elastance at each control step would require continuously integrating the charging equations during the detumbling simulation, significantly increasing computational cost. Future work will investigate efficient reduced-order methods to capture elastance variation during detumbling.

To model the elastance matrix between each spacecraft and electrically isolated component, a Surface Multi-Sphere Model (SMSM) is employed following the Method-of-Moments (MoM) approach described by Reference [16]. Each spacecraft is represented by a set of spheres positioned at the centroids of the triangles from a triangular surface mesh of the spacecraft, as shown in Fig. 3b. In this model, the voltage on the ith sphere depends on both its own charge and capacitance as well as the charge of neighboring spheres and is given by

$$\Phi_i = \frac{1}{4\pi\epsilon_0}\frac{Q_i}{R_i} + \sum_{j=1,j\neq i}^{N}\frac{1}{4\pi\epsilon_0}\frac{Q_j}{r_{i,j}} \tag{7}$$

where Q_i and R_i are the charge and radius of the ith sphere respectively, $r_{i,j}$ is the distance between the ith and jth spheres, and ϵ_0 is the permittivity of free space. For all N spheres in the target-servicer system, this is written as a linear system as shown in the following matrix equation:

$$\begin{bmatrix} \Phi_1 \\ \Phi_2 \\ \vdots \\ \Phi_N \end{bmatrix} = \frac{1}{4\pi\epsilon_0} \begin{bmatrix} 1/R_1 & 1/r_{1,2} & \dots & 1/r_{1,N} \\ 1/r_{2,1} & 1/R_2 & \dots & 1/r_{2,N} \\ \vdots & \vdots & \ddots & \vdots \\ 1/r_{N,1} & 1/r_{N,2} & \dots & 1/R_N \end{bmatrix} \begin{bmatrix} Q_1 \\ Q_2 \\ \vdots \\ Q_N \end{bmatrix} \tag{8}$$

Equations (8) and (5) are equivalent with the only difference being that (8) uses an approximate SMSM elastance matrix. As such, we can apply this approximate elastance matrix to Eq. (6) to approximate voltage rate of change of each component during our charging simulation.

As performed by Hughes et al. in Reference [16], the sphere radii in the SMSM are selected to reproduce the elastance of a high-fidelity Method-of-Moments (MoM) reference solution. The reference MoM solution is computed using the same triangular mesh employed to define the sphere centroids in the SMSM. Plots showing the resulting charge distributions from a MoM reference solution and a corresponding SMSM representation are shown in Fig. 3.

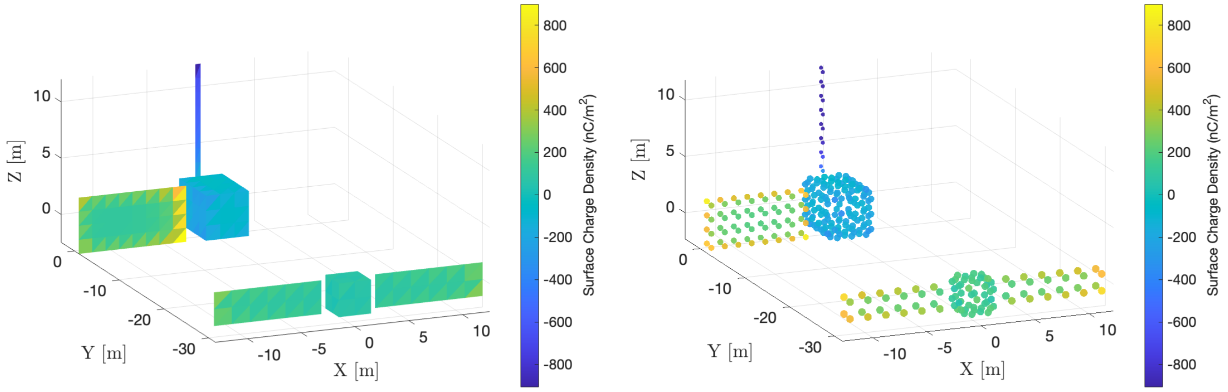

(a) Method of Moments (MOM) Charge Distribution **(b) Surface Multi-Sphere Model (SMSM) Charge Distribution**

Fig. 3 Charge Distribution Modeling Examples

Using the total current on each electrically isolated body from Eq. (1), the SMSM-derived elastance matrix, and the electric potential dynamics from Eq. (6), the evolution of the electric potential distribution of each body is simulated until a steady-state ($\mathrm{d}\boldsymbol{Q}/\mathrm{d}t = 0$) is reached.

B. Touchless Voltage Control Modes

Active control of the target spacecraft's voltage distribution is achieved through a combination of electron-beam charging and targeted UV-induced photoelectron emissions. When the electron-beam is turned on, the servicer emits electrons and charges positively, while the target components absorb electrons and charge negatively. Differential control between the target spacecraft's bus and electrically isolated panel is achieved by illuminating either component with a UV beam to induce localized photoelectron emissions, driving that component's potential to be more positive than the other. This results in six voltage control modes defined by the electron-beam state (on or off), and the UV illumination state (off, illuminating the target panel, or illuminating the target bus). For the uniform potential case, this reduces to four voltage control modes as the bus and panel UV illumination options are combined. Overall, these control modes cover a wide array of differential charging configurations between two target components and the servicer. Table 1 summarizes the expected qualitative voltage trends of each control mode. A "+" indicates a shift toward a more positive potential, "–" indicates a shift toward a more negative potential, and "0" indicates little to no shift from the floating potential.

The required electron-beam and UV-beam parameters needed to achieve kV level differential charging for the detumbling scenario being considered are found in Sec. V.A, and the resulting spacecraft voltage distributions for each

Table 1 Qualitative voltage trends for each charging control mode.

Mode	E-Beam	UV Target	Servicer	Bus	Panel
1	Off	Off	0	0	0
2	On	Off	+	−	−
3	On	Bus	+	+	−
4	On	Panel	+	−	+
5	Off	Bus	0	+	0
6	Off	Panel	0	0	+

control mode are simulated using the differential charging model described in Sec. IV.A and reported in V.B.

For the differential voltage control case, the ability to induce a positive current on the target panel using the UV beam depends on the orientation of the target relative to the servicer: If the panel is oriented away from the servicer, the UV-beam will be blocked by the target bus, and positive voltage control of the panel is not possible. To account for this, a line-of-sight check between the UV-beam origin and a point near the edge of the panel is performed using the Möller–Trumbore ray–triangle intersection algorithm [17]. If an intersection is detected between the UV-beam and any facet of the target bus, the UV panel illumination control mode is disabled.

C. Electrostatic Torque Modeling

To efficiently compute the electrostatic forces and torques between the spacecraft, the same SMSM used for the charge analysis in Sec. IV.A is used. Rather than integrating the Coulomb interactions across all surfaces on each spacecraft, the SMSM approximates these forces as the sum of the forces between each sphere. The Coulomb force on the ith sphere on the target spacecraft due to the jth sphere on the servicer is given by

$$\boldsymbol{F}_i = \sum_{j=1}^{N_s} \frac{1}{4\pi\epsilon_0} \frac{Q_i Q_j}{r_{ij}^3} r_{ij} \tag{9}$$

where Q_i and Q_j are the charges of the ith and jth spheres respectively, $r_{i,j}$ is the distance between the ith and jth spheres, and ϵ_0 is the permittivity of free space. By taking the sum of forces acting on each sphere on the target, the total force and torque acting on the spacecraft are computed using

$$\boldsymbol{F}_{\text{tot}} = \sum_{i=1}^{N_t} \boldsymbol{F}_i \tag{10}$$

$$\boldsymbol{L} = \sum_{i=1}^{N_t} r_{c,i} \times \boldsymbol{F}_i \tag{11}$$

where $r_{c,i}$ is the vector from the spacecraft center of mass to sphere i.

To compute these forces and torques, the charge distribution on all spheres must be known. The charges are related to the voltages through the inverse of Eq. (5). This is shown with a block-structured elastance matrix $[S]$ in

$$\boldsymbol{Q} = [S]^{-1}\boldsymbol{\Phi} = \begin{bmatrix} [S_1] & [S_{1,2}] & [S_{1,s}] \\ [S_{2,1}] & [S_2] & [S_{2,s}] \\ [S_{s,1}] & [S_{s,2}] & [S_s] \end{bmatrix}^{-1} \begin{bmatrix} \Phi_1 \\ \Phi_2 \\ \Phi_s \end{bmatrix} \tag{12}$$

where the target bus, target panel, and servicer self-elastances are $[S_{tb}]$, $[S_{tp}]$, and $[S_s]$ respectively, and the off-diagonal blocks are the mutual-elastance between each component.

Unlike in the differential charging analysis, the elastance matrix is time-varying during the detumbling simulation and must be updated as the target attitude changes. At each time step, the mutual-elastance blocks between the servicer and target spheres are computed based on inter-sphere distances using Eq. (7). Assuming each spacecraft is rigid, the self-elastance blocks of each spacecraft, including the mutual-elastance between the target panel and bus, do not vary with time and can therefore be precomputed using a high-fidelity MoM solution and reused at each timestep.

Direct inversion of $[S]$ at each timestep is computationally expensive. To address this, a Schur complement is applied to reduce the system to the servicer degrees of freedom. The reduced system is then solved efficiently using a

Cholesky decomposition. Once the servicer charges are obtained, the target charges are recovered via back-substitution using the precomputed Cholesky factors of $[S_t]$. This approach is mathematically equivalent to inverting the full elastance matrix but avoids the high computational cost and numerical instability of forming the full inverse at every timestep.

D. Detumbling Control Law

To determine the optimal charge control mode at each control step, a Lyapunov-optimal control law based on the target's rotational kinetic energy is used. The Lyapunov function and its derivative are shown in Eqs. (13) and (14) respectively:

$$V(\boldsymbol{\omega}) = \frac{1}{2}\boldsymbol{\omega}^T[I]\boldsymbol{\omega} \tag{13}$$

$$\dot{V}(\boldsymbol{\omega}) = \boldsymbol{\omega}^T[I]\dot{\boldsymbol{\omega}} = \boldsymbol{\omega}^T([I]\boldsymbol{\omega}\times\boldsymbol{\omega} + \boldsymbol{L_c}) = \boldsymbol{\omega}^T\boldsymbol{L}_c \tag{14}$$

where $\boldsymbol{\omega}$ is the target spacecraft angular velocity in the target body frame, $\boldsymbol{L}_c$ is electrostatic torque in the target body frame, and $[I]$ is the target inertia matrix in the target body frame [18].

At each control step, the estimated electrostatic torque on the target spacecraft for each voltage control discussed in Sec. IV.B is calculated using the SMSM, and the control producing the most negative $\dot{V}$ is selected to maximally reduce the target's kinetic energy, as shown in

$$\boldsymbol{\Phi}^* = \underset{\boldsymbol{\Phi}\in\boldsymbol{\Phi}_{opts}}{\arg\min}\left(\boldsymbol{\omega}^T\boldsymbol{L}_c(\boldsymbol{\Phi})\right) \tag{15}$$

where $\boldsymbol{\Phi}^*$ is the optimal voltage combination at that control step.

Using the Lyapunov function in Eq. (13), which is positive definite, and enforcing $\dot{V}(\boldsymbol{\omega}) \leq 0$ using the above voltage control selection strategy ensures Lyapunov stability of the equilibrium $\boldsymbol{\omega} = 0$. Because the available torques at each time step are discrete and orientation-dependent, a formal proof of global asymptotic stability would require characterizing the invariant set where $\dot{V} = 0$ under control mode switching, which is left to future work. However, for all tested geometries and initial conditions, numerical simulations demonstrate convergence of $\boldsymbol{\omega}(t) \to 0$, indicating asymptotic behavior.

In evaluating the Lyapunov function, it is assumed that the servicer has perfect knowledge of the target spacecraft's angular rates through sensors such as LIDAR. Further it is assumed that the target center of mass and inertia properties are known or can be accurately approximated, and the servicer is capable of accurately estimating the differential voltage distribution and thus the center of charge for each control mode.

E. Attitude Dynamics

The attitude of the target spacecraft is parameterized using scalar-first quaternions, and its body-frame angular rates are integrated using the Euler rotational equations of motion:

$$[I]\dot{\boldsymbol{\omega}} = -[\tilde{\boldsymbol{\omega}}][I]\boldsymbol{\omega} + \boldsymbol{L}_c \tag{16}$$

where $[I]$ is the target spacecraft moment of inertia, and $\boldsymbol{L}_c$ is the total electrostatic torque on the target spacecraft taken about its center of mass. The spacecraft attitude is then integrated using the quaternion kinematic differential equations:

$$\begin{bmatrix}\dot{\beta}_0\\ \dot{\beta}_1\\ \dot{\beta}_2\\ \dot{\beta}_3\end{bmatrix} = \frac{1}{2}\begin{bmatrix}0 & -\omega_1 & -\omega_2 & -\omega_3\\ \omega_1 & 0 & \omega_3 & -\omega_2\\ \omega_2 & -\omega_3 & 0 & \omega_1\\ \omega_3 & \omega_2 & -\omega_1 & 0\end{bmatrix}\begin{bmatrix}\beta_0\\ \beta_1\\ \beta_2\\ \beta_3\end{bmatrix} \tag{17}$$

where ω_1, ω_2, and ω_3 are the inertial body-frame angular rates and β_0, β_1, β_2, and β_3 are the components of the scalar-first quaternion.

V. Results

A. Electron-Beam and UV-Light Parameter Selection

To enable the differential voltage control modes described in Sec. IV.B, appropriate electron-beam and UV-light parameters must be selected. For the electron-beam, the primary design variables are the beam energy and beam current.

The beam energy determines the maximum achievable potential difference between the servicer and target while the beam current directly contributes to the net charging current on each conducting body. For the UV illumination, the key parameters are the photon wavelength and the optical power, which together determine the photon flux and resulting photoelectron emission rate.

Two charging studies are performed for the differential charging case to select these parameters. In both studies, a planetary K_p index of 0 and a local time of 1200 is assumed, and the corresponding plasma environment data for GEO is taken from Denton et al. in Reference [19]. A solar photoelectron flux of 20 μA/m^2 is used with a photoelectron temperature of 2 eV. All spacecraft surfaces are assumed to be aluminum, and the backscattered, secondary, and photoelectron yields of Aluminum are used. The sunlit area of each electrically isolated component is set to its maximum possible value. The servicer spacecraft is assumed to absorb all secondary, backscattered, and photoemitted electrons originating from the target. For the SMSM elastance model, the target spacecraft is represented using 212 spheres while the servicer is represented using 96 spheres.

Electron-Beam Parameter Study

The first study determines the required beam energy and beam current for the control modes in which both target components receive electron-beam current and no UV illumination is used. A beam energy of 20 kV is selected, and the beam current is varied from 0.5 to 2.0 mA. The resulting steady-state potentials of the target bus, target panel, and servicer are shown in Fig. 4.

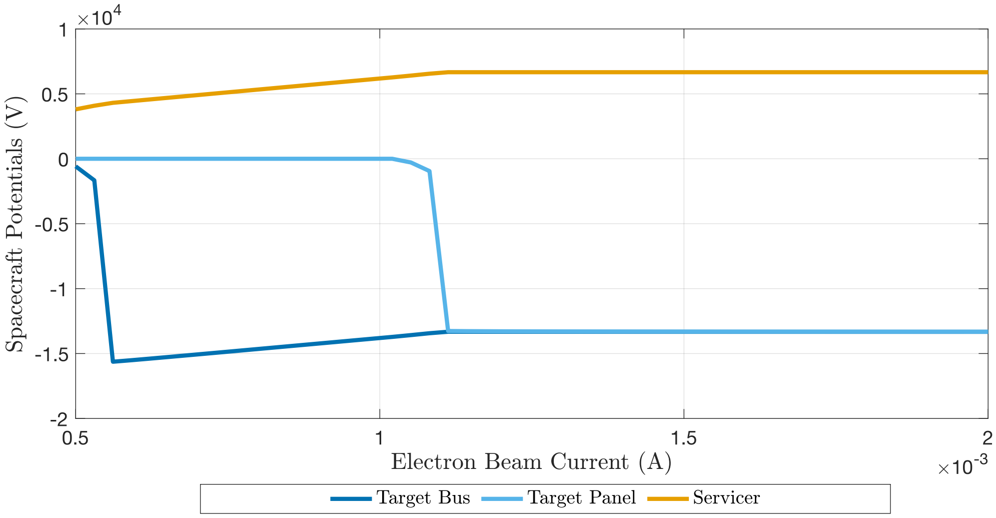

Fig. 4 Spacecraft Potentials (V) vs. Electron Beam Current (A)

These results indicate that a current of approximately 1.1 mA is required to drive both the bus and panel to negative potentials. These results also show that the bus reaches negative potentials at lower beam currents than the panel, and this can be explained by its smaller sunlit area: in GEO, solar UV–induced photoemission tends to dominate the current balance and drives surfaces toward a small positive floating potential. Because the panel has a larger sunlit area and receives more solar UV flux, a larger electron-beam current is required to overcome the solar photoemission current. Based on this study, the electron-beam current is set to 1.1 mA. For a beam energy of 20 kV, this corresponds to a beam power of 22 W, matching the beam power used in previous electrostatic detumbling work [7].

UV-Beam Parameter Study

The second study identifies the UV-beam parameters needed to produce differential charging when the electron-beam is active. As discussed in Sec. IV.A, photoelectron emission increases with photon energy, so a wavelength of 190 nm (6.5 eV) is selected, corresponding to a quantum yield of 3×10^{-4} photoelectrons per incident photon [20]. This wavelength is within the high-energy range available from commercial off-the-shelf (COTS) UV lasers [13]. With the wavelength fixed, the UV-beam power becomes the remaining design variable. For both the bus-illumination and panel-illumination control modes, the UV-beam power is varied from 0.5 to 10 W, and the resulting steady-state potentials are shown in Fig. 5.

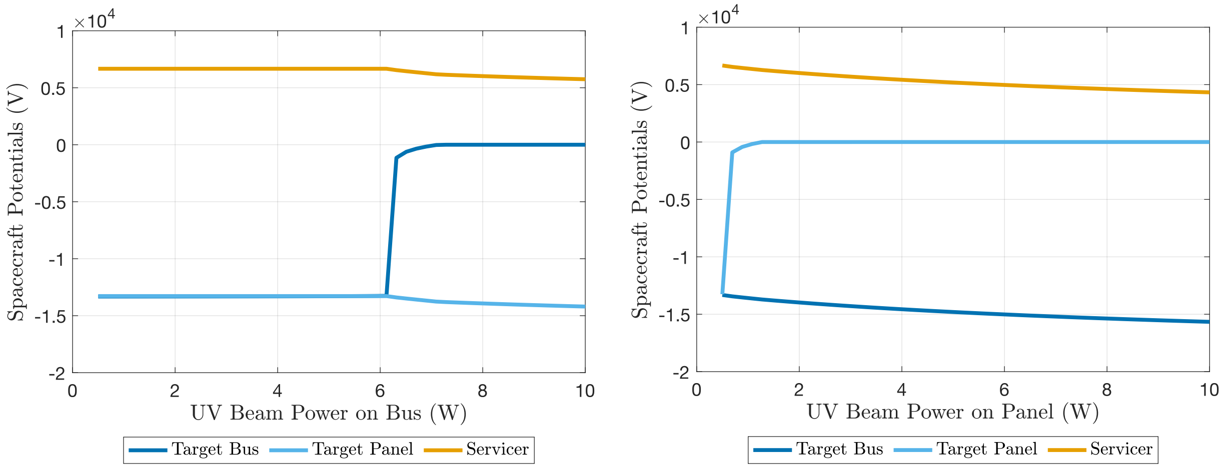

(a) Target Bus Illumination

(b) Target Panel Illumination

Fig. 5 Spacecraft Potentials (V) vs. UV Beam Power (W) during Illumination of Target Bus or Panel and Electron Beam Operation.

These results indicate that a UV power of roughly 7 W is required to generate a large voltage difference between the target bus and panel in both illumination cases. These results also show that the bus requires higher UV power than the panel, and this is likely a result of the chosen electron-beam current: Because the electron-beam current chosen corresponds to the minimum current needed to drive both components to a negative potential, and the panel required a larger current to overcome its solar photoelectron current, a lower UV-beam induced current is needed to drive the panel back to a positive value. From these results, the UV-beam power is set to 7 W. Although this exceeds the output of most COTS UV lasers (typically below 50 mW [13]), it could be achieved through the use of multiple UV light sources. Additionally future work will consider the differential charging possible using realistic powers from COTS UV sources.

B. Control Mode Voltages

Using the electron-beam and UV-beam parameters selected in Sec.V.A, the steady-state electric potentials produced by each charging control mode are computed using the differential charging model in Sec. IV.A with the initial potential distribution corresponding to the natural floating potential of each component. For each mode, the total current balance in Eq. (1) is integrated together with the SMSM-derived elastance model until a steady-state voltage is reached. The resulting equilibrium voltages represent the steady potentials that each control mode imposes on the target bus, target panel, and servicer spacecraft.

Tables 2 and 3 summarize the computed steady-state potentials for the differential and uniform charging cases respectively with each row corresponding to one of the control modes defined in Sec. IV.B.

Table 2 Steady-State Potentials [V] for Differential Charging Case.

Control Mode	Target Bus Potential [V]	Target Panel Potential [V]	Servicer Potential [V]
Natural Floating	3.4609	5.4154	4.9535
E-beam On, UV Off	−13 320.3260	−13 255.0359	6666.4747
E-beam On, UV on Bus	0.0597	−13 821.9648	6099.1173
E-beam On, UV on Panel	−15 332.6050	0.8381	4654.1221
E-beam Off, UV on Bus	5.1543	5.4154	4.2521
E-beam Off, UV on Panel	3.4609	6.4046	4.5480

Table 3 Steady-State Potentials [V] for Uniform Charging Case.

Control Mode	Target Potential [V]	Servicer Potential [V]
Natural Floating	4.5543	4.9535
E-beam On, UV Off	−13 307.0869	6666.6025
E-beam On, UV On	−146.3102	5943.1043
E-beam Off, UV On	5.2730	4.2865

These steady-state voltages are used as the voltage inputs for the SMSM force and torque computations used in the optimal detumbling control and dynamical simulations described in Secs. IV.C and IV.E.

C. Detumbling Results

To compare the detumbling performance between the uniform and differential charging, both cases are simulated under the same initial target tumbling scenario. In this scenario, the target spacecraft is tumbling about its body frame 3-axis at a rate of 2 deg/s. The body frame is initially aligned with the Hill frame, so the initial rotation is effectively about the Hill frame Z axis. The target spacecraft's moment of inertia tensor components in the body frame is:

$$^{\mathcal{B}}[I] = \begin{bmatrix} 5.7252\times10^{3} & -5.4938\times10^{1} & 1.6452\times10^{2} \\ -5.4938\times10^{1} & 1.1783\times10^{4} & -2.7581\times10^{2} \\ 1.6452\times10^{2} & -2.7581\times10^{2} & 1.3640\times10^{4} \end{bmatrix} (\mathrm{kg}\cdot\mathrm{m}^2) \tag{18}$$

This inertia was calculated from the dry mass and simplified GOES-R geometry assuming a uniform surface mass distribution. It is important to note that the target body frame is not aligned with the principal inertia axes of the target. As a result, there are non-zero off-diagonal terms in the body frame inertia matrix, and the nominal 2 deg/s spin about the body frame 3-axis is not a principal-axis rotation, leading to natural oscillations in the torque free motion. In the SMSM electrostatic force and torque model, the target spacecraft is represented using 212 spheres while the servicer is represented using 96 spheres.

Using the electrostatic force and torque model, detumbling control law, and attitude dynamics described in Secs. IV.C, IV.D, and IV.E along with the uniform and differential control voltages found in Sec. V.B, electrostatic detumbling is simulated for 500 hours (approximately 3 weeks). In the simulation, when all body angular rates are reduced to below 0.05 deg/s, the servicer is assumed to move to a separation distance where electrostatic interactions become negligible, marking a successful detumbling. The time histories of the target angular rates, rotational kinetic energy, and electrostatic torques for both the uniform and differential voltage cases are shown in Fig. 6, Fig. 7, and Fig. 8 respectively.

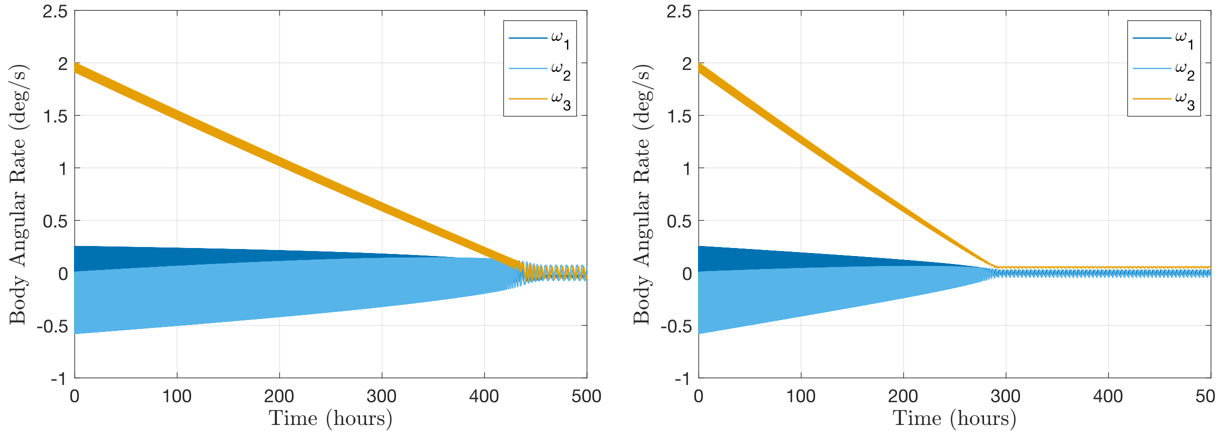

(a) Uniform Target Voltage Case.

(b) Differential Target Voltage Case.

Fig. 6 Body Angular Rate (deg/s) vs. Time (hours) for Uniform and Differential Target Voltage Cases with initial spin of 2 deg/s about body 3-axis.

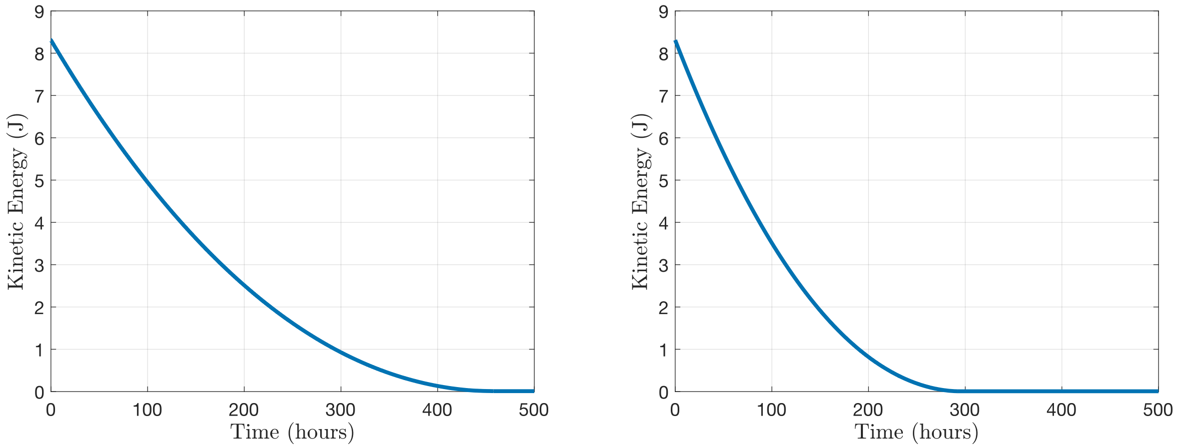

(a) Uniform Target Voltage Case.

(b) Differential Target Voltage Case.

Fig. 7 Target Rotational Kinetic Energy (J) vs. Time (hours) for Uniform and Differential Target Voltage Cases with initial spin of 2 deg/s about body 3-axis.

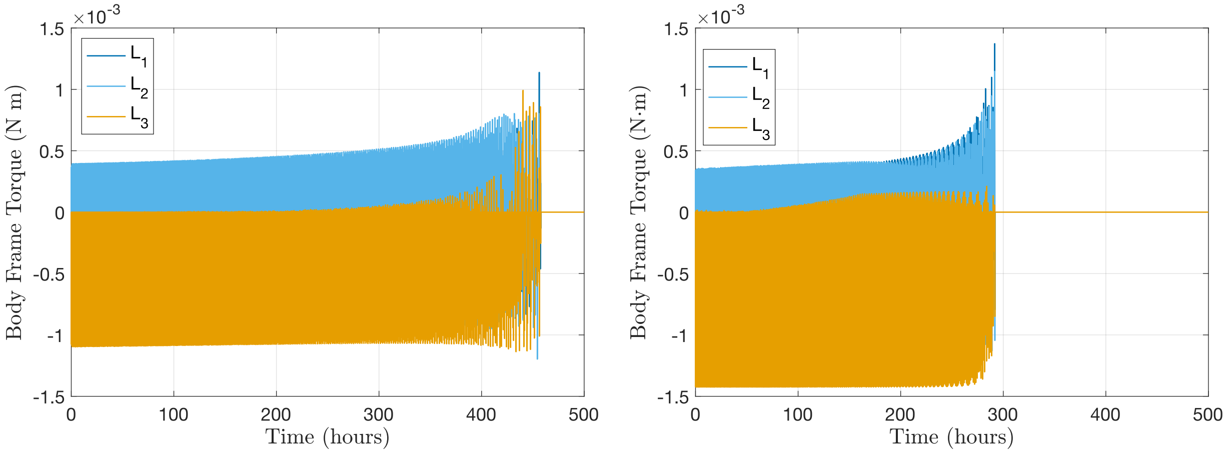

(a) Uniform Target Voltage Case.

(b) Differential Target Voltage Case.

Fig. 8 Body Frame Electrostatic Torques (N · m) vs. Time (hours) for Uniform and Differential Target Voltage Cases with initial spin of 2 deg/s about body 3-axis.

The simulation results demonstrate that the ability to produce differential voltages on a target spacecraft significantly improves electrostatic detumbling performance compared to a target with a uniform voltage distribution. For the same spacecraft geometries, electron-beam and UV-beam parameters, and initial tumbling state, the differential case reduces the detumbling time from roughly 450 hours to under 300 hours, yielding an improvement of approximately 6.25 days.

As shown in Fig. 6, both control strategies successfully drive all three body angular rates to zero. However, the differential case reduces the body 3-axis rate more rapidly while also reducing the cross-coupled oscillations in the 1- and 2-axes earlier. The evolution of the rotational kinetic energy is consistent with this behavior: In Fig. 7, the differential voltage case reduces the rotational kinetic energy at a faster rate, indicating that the electrostatic torques available for the voltage control modes are either stronger or about a more favorable axis than the uniform case. This matches the results shown by the torque time histories shown in Fig. 8 where the magnitude of the torque about the body frame 3-axis is larger for the differential case than the uniform case for the target attitudes encountered during the detumbling process. The apparent increase in torques about the body 1- and 2-axes are due the available torques changing as the target orientation evolves and the controller shifting to reducing spin about these axes once the 3-axis spin has been sufficiently reduced.

Overall, these results indicate that differential voltage control can enhance the electrostatic torques available during detumbling and substantially improve electrostatic detumbling times. This capability is particularly valuable in GEO where large, high-moment-of-inertia targets such as the GOES-R spacecraft modeled here, can have detumbling times on the order of weeks for initial tumbling rates of just $1-2$ deg/s.

VI. Conclusion

This work develops and evaluates an electrostatic detumbling strategy for spacecraft with electrically isolated surfaces using active differential charge control. A differential charging model combining a Surface Multi-Sphere Model elastance representation with analytic current balance equations is used to predict steady-state voltages produced a combination of control modes using an electron-beam and targeted UV illumination. These voltages are then used in a Surface Multi-Sphere Model electrostatic torque model and a Lyapunov-optimal control law to simulate touchless detumbling of a target modeled after the GOES-R spacecraft.

The results of these simulations demonstrate that controlling differential voltages across target components can enhance the electrostatic torques available during detumbling by shifting the location of the effective center of charge and generating attractive and repulsive forces on different parts of the structure. For the GEO environment and beam parameters investigated, the differential-voltage control reduced the simulated detumbling time from roughly 450 hours in the uniform voltage case to about 300 hours for an initial tumble of 2 deg/s. These findings indicate that differential voltage control can produce more favorable electrostatic detumbling torques than uniform charging, offering an improvement in detumbling performance for large spacecraft in GEO.

Future work will focus on incorporating several charging effects that were not modeled in the present study including field emissions and consideration of electrostatic discharge risk, both of which are increasingly relevant for the kilovolt-level surface potentials modeled in this paper. Additionally, a UV-beam induced current model considering the effects of reflectance and incidence angle will be implemented. Finally, additional studies evaluating differential detumbling performance for varying space weather environments and target material properties will be performed.

Acknowledgements

This work was supported by the U.S. Air Force Office of Scientific Research under grant FA9550-23-S-0570. During the preparation of this work, the authors used ChatGPT solely to assist with proofreading of the manuscript. All technical content, analysis, and conclusions are entirely the work and responsibility of the authors.

References

[1] Zhang, H., Li, Z., Wang, W., Zhang, Y., and Wang, H., "Geostationary Orbital Debris Collision Hazard after a Collision," Vol. 9, No. 5, 2022, p. 258. https://doi.org/10.3390/aerospace9050258.

[2] Oltrogge, D. L., Alfano, S., Law, C., Cacioni, A., and Kelso, T. S., "A Comprehensive Assessment of Collision Likelihood in Geosynchronous Earth Orbit," Vol. 147, 2018, pp. 316–345. https://doi.org/10.1016/j.actaastro.2018.03.017.

[3] Couzin, P., Rembala, R., Teti, F., Bakouche, C., and Billot, C., "Active Removal of Large Debris: System Approach of Desorbiting Concepts and Technological Issues," 2013. URL https://conference.sdo.esoc.esa.int/proceedings/sdc6/paper/25.

[4] Gangapersaud, R. A., Liu, G., and De Ruiter, A. H., "Detumbling of a Non-Cooperative Target with Unknown Inertial Parameters Using a Space Robot," Vol. 63, No. 12, 2019, pp. 3900–3915. https://doi.org/10.1016/j.asr.2019.03.002.

[5] Xu, W., Liang, B., Li, B., and Xu, Y., "A Universal On-Orbit Servicing System Used in the Geostationary Orbit," Vol. 48, No. 1, 2011, pp. 95–119. https://doi.org/10.1016/j.asr.2011.02.012.

[6] Papushev, P., Karavaev, Y., and Mishina, M., "Investigations of the Evolution of Optical Characteristics and Dynamics of Proper Rotation of Uncontrolled Geostationary Artificial Satellites," Vol. 43, No. 9, 2009, pp. 1416–1422. https://doi.org/10.1016/j.asr.2009.02.007.

[7] Bennett, T., Stevenson, D., Hogan, E., and Schaub, H., "Prospects and Challenges of Touchless Electrostatic Detumbling of Small Bodies," Vol. 56, No. 3, 2015, pp. 557–568. https://doi.org/10.1016/j.asr.2015.03.037.

[8] Bennett, T., and Schaub, H., "Touchless Electrostatic Detumble of a Representative Box-and-Panel Spacecraft Configuration," 2017. URL https://conference.sdo.esoc.esa.int/proceedings/sdc7/paper/1000.

[9] Casale, F., Schaub, H., and Douglas Biggs, J., "Lyapunov Optimal Touchless Electrostatic Detumbling of Space Debris in GEO Using a Surface Multisphere Model," Vol. 58, No. 3, 2021, pp. 764–778. https://doi.org/10.2514/1.A34787.

[10] Sarno-Smith, L. K., Larsen, B. A., Skoug, R. M., Liemohn, M. W., Breneman, A., Wygant, J. R., and Thomsen, M. F., "Spacecraft Surface Charging Within Geosynchronous Orbit Observed by the Van Allen Probes," Vol. 14, No. 2, 2016, pp. 151–164. https://doi.org/10.1002/2015SW001345.

[11] Olsen, R. C., McIlwain, C. E., and Whipple Jr., E. C., "Observations of Differential Charging Effects on ATS 6," Vol. 86, No. A8, 1981, pp. 6809–6819. https://doi.org/10.1029/JA086iA08p06809.

[12] Romero-Calvo, A., Hammerl, J., and Schaub, H., "Touchless Potential Sensing of Differentially Charged Spacecraft Using Secondary Electrons," Vol. 59, No. 5, 2022, pp. 1623–1633. https://doi.org/10.2514/1.A35355.

[13] Romero-Calvo, A., Champion, K., and Schaub, H., "Enabling Ultraviolet Lasers for Touchless Spacecraft Potential Sensing," Vol. 51, No. 9, 2023, pp. 2468–2481. https://doi.org/10.1109/TPS.2023.3264914.

[14] Lai, S. T., *Fundamentals of Spacecraft Charging*, Princeton University Press, 2012.

[15] Hammerl, J., and Schaub, H., "Reduced Order Spacecraft Charging Models for Electrostatic Proximity Operations," Vol. 52, No. 11, 2024-11, pp. 5402–5413. https://doi.org/10.1109/TPS.2024.3503356.

[16] Hughes, J. A., and Schaub, H., "Heterogeneous Surface Multisphere Models Using Method of Moments Foundations," Vol. 56, No. 4, 2019, pp. 1259–1266. https://doi.org/10.2514/1.A34434.

[17] Möller, T., and Trumbore, B., "Fast, Minimum Storage Ray-Triangle Intersection," Vol. 2, No. 1, 1997, pp. 21–28. https://doi.org/10.1080/10867651.1997.10487468.

[18] Schaub, H., and Junkins, J. L., *Analytical Mechanics of Space Systems, Fourth Edition*, American Institute of Aeronautics and Astronautics, Inc., 2018. https://doi.org/10.2514/4.105210.

[19] Denton, M. H., Thomsen, M. F., Korth, H., Lynch, S., Zhang, J. C., and Liemohn, M. W., "Bulk Plasma Properties at Geosynchronous Orbit," Vol. 110, No. A7, 2005. https://doi.org/10.1029/2004JA010861.

[20] Feuerbacher, B., and Fitton, B., "Experimental Investigation of Photoemission from Satellite Surface Materials," Vol. 43, No. 4, 1972-04-01, pp. 1563–1572. https://doi.org/10.1063/1.1661362.